This is a repository copy of *Aspects of the internal physics of InGaAs/InAlAs quantum cascade lasers* .

White Rose Research Online URL for this paper:
http://eprints.whiterose.ac.uk/1697/

Aspects of the internal physics of InGaAs/InAlAs quantum cascade lasers

James Mc Tavish[a)]
*School of Electronic and Electrical Engineering, The University of Leeds, Leeds LS2 9JT,
United Kingdom and School of Engineering, Liverpool John Moores University, Byrom Street,
Liverpool L3 3AF, United Kingdom*

Dragan Indjin and Paul Harrison
*School of Electronic and Electrical Engineering, The University of Leeds, Leeds LS2 9JT,
United Kingdom*

We report on the results of our simulations of an InGaAs/InAlAs midinfrared quantum cascade laser (QCL) designed to operate in continuous wave mode at room temperature [Beck *et al.*, Science **295**, 301 (2002)]. Our physical model of the device consists of a self-consistent solution of the subband population rate equations and accounts for all electron-longitudinal-optical phonon and electron-electron scattering rates, as well as an evaluation of the temperature of the nonequilibrium electron distribution. We also consider the role of the doping density and its influence on the electron dynamics. We found that the temperature of the nonequilibrium electron distribution differed significantly from the lattice temperature and that this temperature increased with applied electric field and current density, with coupling constants somewhat larger than analogous GaAs based midinfrared QCLs. Our simulations also reveal physical processes of the device that are not apparent from the experimental measurements, such as the role of electron-electron scattering. © *2006 American Institute of Physics*. [DOI: 10.1063/1.2201252]

I. INTRODUCTION

The quantum cascade laser (QCL) is an electrically pumped semiconductor laser that emits in the midinfrared region of the electromagnetic spectrum. Unlike most semiconductor injection lasers that make use of electron-hole recombination to generate electromagnetic radiation, QCLs are unipolar devices that utilize intersubband transitions in a repetition of identically coupled multi-quantum-well structures.[1–3]

The first experimental realization of a QCL was demonstrated in 1994 by Faist *et al.* at Bell Laboratories, Lucent Technologies,[1] some 20 years after the theoretical predictions by Kazarinov and Suris[4,5] of electrically pumped intersubband optical amplifiers. Since then there has been tremendous progress in QCL research, which has resulted in bidirectional,[6] multiwavelength,[6,7] ultrabroadband,[8] above room-temperature continuous operation,[9–11] operation in the terahertz region,[12] sum-frequency and higher order harmonic generation,[13–15] and fully integrated electrically pumped Raman lasers.[16]

For further improvements a detailed knowledge of the crucial design parameters, as well as an understanding of the relevant physical limitations of particular designs, it is highly desirable to investigate the influences of the relevant physical and technological parameters. The doping level in the active region is one such important parameter that has particular significance on the dynamic range of QCLs. Until now, very few experimental investigations have been presented that have discussed the influence of the injector doping on QCL threshold currents.[17–19]

In this work we report on such a theoretical investigation of a recent four-quantum-well design,[9] in which the influence of the injector doping density on the electron dynamics and on the carrier heating is analyzed.

Beck *et al.*,[9] reported on the design of a midinfrared semiconductor laser that provided 3 mW of continuous optical power at a lasing wavelength of 9.18 μm and an operating temperature of 312 K. Figure 1 shows the moduli-squared wave functions for two periods of the device when band nonparabolicity, described via a two band Kane model, is taken into account (see Hirayama *et al.*[20]) for a value of the electric field of $F=43$ kV/cm (the working field as estimated from the current-voltage characteristics of Beck *et al.*). The structure is formed from alternate In$_{0.52}$Al$_{0.48}$As barriers and In$_{0.53}$Ga$_{0.47}$As wells that make up four regions, the active region followed by an injector region (which together are taken to form one period of the device), itself followed by another active and injector region. The laser transition takes place between the active region levels la-

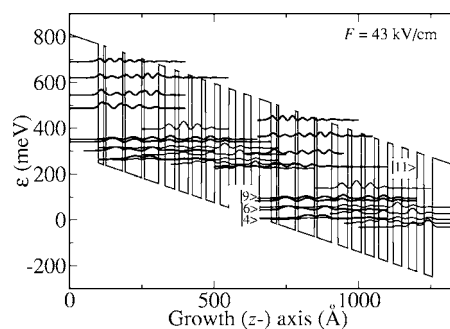
FIG. 1. The QC structure of Beck *et al.* showing two periods and the moduli-squared wave functions for an applied electric field $F=43$ kV/cm.

[a)]Electronic mail: j.p.mctavish@livjm.ac.uk

beled $|11\rangle$ and $|9\rangle$ in the figure, with the levels $|6\rangle$ and $|4\rangle$ providing rapid depopulation from the lower laser level, $|9\rangle$, via electron-longitudinal-optical (e-LO) phonon scattering between the levels $|9\rangle \rightarrow |6\rangle$ and $|6\rangle \rightarrow |4\rangle$ (the labeling of levels is based on the full set of solutions obtained, and the levels $|11\rangle$, $|9\rangle$, $|6\rangle$, and $|4\rangle$ correspond to the levels $|4\rangle$, $|3\rangle$, $|2\rangle$, and $|1\rangle$ discussed by Beck *et al.*). This mechanism is efficient because the energy separation between these levels is close to the 34 meV LO phonon energy for the $In_{0.53}Ga_{0.47}As$ well material.[21]

These electrons are then reinjected into the adjacent region, via the coupling provided by the presence of injector region miniband states, where a further laser transition takes place. Thus, the significance of the QC structure is that since layers are arranged periodically, the active region level of one period is connected to the upper laser level of the next period.

The quaternary $In_{1-x-y}Al_xGa_yAs$ has become an important material for intersubband lasers because of its large conduction band (CB) offset. In particular, the specific alloy concentrations $In_{0.52}Al_{0.48}As$ and $In_{0.53}Ga_{0.47}As$ are of importance because they are lattice matched to the readily available substrates and therefore introduce no strain.[22]

In this report we discuss the results of our simulations for a range of lattice temperatures and doping densities, solving for the scattering rates in a self-consistent manner, including both e-LO and electron-electron (e-e) scattering processes[23–26] as well as for the temperature of the nonequilibrium electron distribution.[23,27] This gives insight into the internal physics of the devices: An improved understanding may influence future designs.

II. MODELING

Carrier transport within the quantum cascade structure is described within a tight-binding-like picture, where any state in the long cascade is associated with one of its periods. Because of the quasiperiodicity of the structure, if $\psi(z)$ is a solution of the Schrödinger equation with energy ε, then $\psi(z-D)$ is a solution with energy $\varepsilon - \Delta V$, where D is the periodicity of the structure and ΔV is the potential energy drop across one period. This allows all the states in a cascade to be constructed as replicas, shifted in space and energy, of the set of initial states. Among the states actually calculated in a structure with a finite set of periods, those that are mostly localized near the middle of the structure are the most representative of states in an infinite cascade structure, because they are sufficiently remote from the boundaries and are used in the replication process.[28,29]

Heterostructures consist of alternate layers of dissimilar material so that the mass of the carrier is different in these layers, and to solve the Schrödinger equation we adopt the envelope function approximation:[24]

$$\left\{ -\frac{\hbar^2}{2}\frac{d}{dz}\left[\frac{1}{m^*(z)}\frac{d}{dz}\right] + V(z) \right\}\psi_n(z) = \varepsilon_n\psi_n(z), \qquad (1)$$

where the integer n labels the subbands and $V(z)$ is the band discontinuity at the well/barrier interface. A uniform electric field F along the growth direction z may be allowed for by

replacing the potential $V(z)$ in Eq. (1) by $V(z) + qFz$, where for an electron $q = -e$ and e is the magnitude of the charge on the electron.

III. SELF-CONSISTENT APPROACH

We start from the expression for the rate of increase of the population of the ith level,

$$\frac{dn_i}{dt} = +\sum_{f\neq i} n_f w_{fi} - \sum_{f\neq i} n_i w_{if}, \qquad (2)$$

where i,f run over all states and over all periods and w_{fi} is the rate at which particles make the transition $f \rightarrow i$ which increase the population of level i and is identified with $1/\tau_{fi}$, where τ_{fi} is the carrier scattering time, and similarly w_{if} is the rate at which particles make the transition $i \rightarrow f$ which depopulate the level i and is identified with $1/\tau_{if}$.

The major inelastic scattering mechanism in InGaAs/InAlAs systems is via the electron-longitudinal-optical phonon interaction, and in the calculation of the scattering rates, the processes of emission and absorption of these polar optical phonons were taken into account, assuming bulklike phonon modes.

Carrier-carrier scattering (the Auger interaction) is also an important mechanism in QCLs, particularly in those devices with closely spaced subbands, and we include this mechanism in determining the scattering rates.[30]

In principle the summation in Eq. (2) is taken over all possible states f from all the regions that make up the device. In practice this would be computationally prohibitive and the summation is taken only over two periods, together with suitable assumptions regarding the subband populations and the transition rates due to the quasiperiodicity of the structure.[23,29,31]

Assuming that all the levels are in the steady state, we have $dn_i/dt = 0$ giving

$$\sum_{f\neq i} n_f w_{fi} - \sum_{f\neq i} n_i w_{if} = 0, \qquad (3)$$

and then we can, in principle, solve for n_i when we make use of the constraint $\sum_i n_i = N$, where N is the total carrier density. Note that the scattering rates also depend on the population of the levels n_i,[26] so that Eq. (3) is a nonlinear problem which suggests a solution using an iterative scheme that is run until self-consistency is achieved.[23]

We refine the model by taking into account the subband exchange energy, as well as particles, in all scattering processes (elastic or inelastic). The effect of this is to introduce a carrier temperature T_e that differs from the lattice temperature T_l. Recent experimental and theoretical works[27,32] justify the use of a single (average) electron temperature as a good approximation in midinfrared QCLs. The final form of the single temperature balance equation reads[29]

$$\Delta = \sum_{em,abs,ee} \sum_{i,f} n_f w_{fi}(\varepsilon_f - \varepsilon_i + \delta E) = 0, \qquad (4)$$

where $\varepsilon_f - \varepsilon_i$ is the subband energy separation and the change in energy δE is equal to $-E_{LO}$ for phonon emission (em),

TABLE I. Single particle estimates compared with self-consistent scattering times for e-LO scattering.

	Single particle estimates		Self-consistent results	
	Emission	Absorption	Emission	Absorption
$\tau_{11,9}$ (ps)	1.20	6.84	7.06	39.08
$\tau_{11,6}$ (ps)	4.11	18.85	3.75	18.95
$\tau_{11,4}$ (ps)	4.10	17.93	6.24	30.12
$\tau_{9,6}$ (ps)	2.23	11.45	1.12	7.55
$\tau_{9,4}$ (ps)	2.51	11.60	2.23	12.12

$+E_{LO}$ for phonon absorption (abs), and zero for electron-electron (ee) scattering.

Equations (3) and (4) constitute the "self-consistent energy balance" model, and to solve for the subband densities n_i and the average electron temperature T_e we use an iterative procedure.[27,33]

IV. RESULTS AND DISCUSSION

We considered several doping densities in the range $1.0 \times 10^{17} \leqslant N_d \leqslant 2.5 \times 10^{17}$ cm^{-3} [corresponding to sheet densities $(10.3-25.75) \times 10^{10}$ cm^{-2}, respectively] and lattice temperatures $T_l = 77$ and 300 K, with a range of applied electric fields 5 kV/cm $\leqslant F \leqslant 46.5$ kV/cm. We note that the results reported by Beck *et al.* correspond to a doping density of 2×10^{17} cm^{-3} (giving a sheet density of 20.6×10^{10} cm^{-2}), temperatures around 300 K, and applied electric fields around the estimated working field of 43 kV/cm.

Often quoted are the single particle estimates for the scattering rates. These are determined by estimating the populations for the levels and then solving for the scattering rates for these populations. Table I shows our results for the single particle estimates for the emission and absorption scattering times determined from a simplified Beck structure involving only the four quantum-well active region. In this approach we solved Eq. (1) for the simplified structure and make simple estimates for the subband populations of the relevant levels. Our results are in reasonable agreement with the commonly accepted values, especially in the identification of the upper and lower laser levels, for example, see Ref. 9, who quote for the emission scattering times, $\tau_{11,9(e)} = 1.88$ ps, $\tau_{11,6(e)} = 1.92$ ps, $\tau_{11,4(e)} = 2.51$ ps, $\tau_{9,6(e)} = 0.73$ ps, and $\tau_{9,4(e)} = 0.23$ ps.

Also shown in Table I are the values obtained from our calculations with self-consistently determined populations (based upon a total sheet density of 20.6×10^{10} cm^{-2} and a lattice temperature of 300 K). Inspection of Table I shows noticeable disagreement between the single particle estimates and the results of our self-consistent calculations. This is because the lifetimes are strong functions of the carrier densities.

Figure 2 shows the populations for the subbands of interest, i.e., $|11\rangle$, $|9\rangle$, $|6\rangle$, and $|4\rangle$, for the range of electric fields $40.0 \leqslant F \leqslant 46.5$ kV/cm and for a doping density of $N_d = 2 \times 10^{17}$ cm^{-3}; the results for the other doping densities investigated show similar trends.
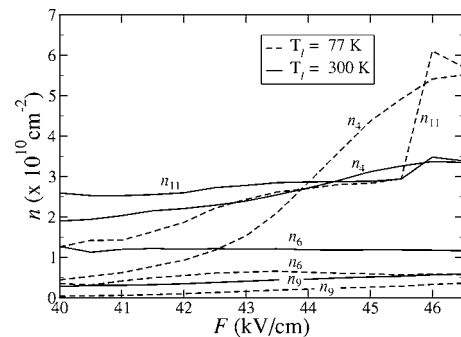

FIG. 2. Variation of the subband populations with applied electric field for a doping density $N_d = 2 \times 10^{17}$ cm^{-3}. Note $|11\rangle$ is the upper laser level, $|9\rangle$ the lower laser level, and $|6\rangle$ and $|4\rangle$ are the relevant active region levels necessary for operation (see the discussion in Ref. 9).

As expected, the population of the lower laser level, $|9\rangle$, is small which is reasonable because of the fast depopulation of that level. We also note that the population of level $|6\rangle$ is comparable to that of level $|9\rangle$, but that the population of level $|4\rangle$ is approximately five times larger than these and of comparable magnitude with the population of the upper laser level. Also noteworthy is that the population of level $|4\rangle$ is larger than the upper laser level for a small range of applied fields.

We now determine the current density J by considering the rate of flow of electrons across some reference plane, for example, the plane separating two periods. It is straightforward to derive

$$J = q\left(\sum_{i=\text{2nd period}} \sum_{f=\text{1st period}} n_i w_{if} - \sum_{i=\text{1st period}} \sum_{f=\text{2nd period}} n_i w_{if} \right), \quad (5)$$

where q is the magnitude of the electron charge and w_{if} is the scattering rate for the transition $i \rightarrow f$, so that the first double sum in Eq. (5) determines the contribution to the current density from the second to the first period while the second double sum is the contribution from the first to the second period, i.e., back-scattering. Our results for the current density are shown in Fig. 3.

Figure 3 shows the results for the current density profile for a lattice temperature of 300 K, with the result for 77 K shown as an inset. From these results we note the abrupt
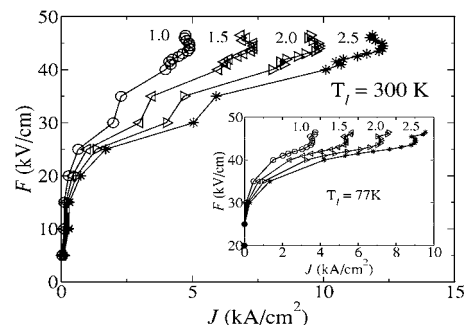

FIG. 3. The variation of the current density profile with doping density for a lattice temperature of 300 K (inset shows results for 77 K). The doping densities are marked in the figure in units of 10^{17} cm^{-3}.

drop in the current density for applied electric fields around 25 kV/cm, followed by a general increase for electric fields above this. Notice the evidence of "negative differential resistance" (NDR) present for all doping densities, but more pronounced for the larger densities, for $F \approx 43$ kV/cm for 300 K, but difficult to discern for 77 K.[34]

We also note the presence of NDR at the smaller applied fields around 30–35 kV/cm, again with less pronounced behavior at the smaller lattice temperatures. This behavior is related to the lining up of the upper laser level with injector levels in the next period and that it occurs for a variety of fields should come as no surprise.

The figure also shows an increase of current with doping density, partially reflecting that larger doping densities means more carriers, hence improving the dynamic working range of the QCL.

From the figure, assuming room-temperature operation of 300 K, a doping density of $N_d = 2 \times 10^{17}$ cm^{-3}, and a working field of approximately 43 kV/cm, we note our calculations to give current saturation at approximately 10 kA/cm^2 compared to 5 kA/cm^2 in experiment.[9]

Referring back to Fig. 2, we note the rapid variation in the population of the upper laser level, n_{11}, around the applied electric fields $F = 45.5–46.0$ kV/cm (with the larger variation at the lower lattice temperature). This variation takes place at around those fields where we have noted the appearance of NDR. This may be expected since from Eq. (5), the current density involves the populations of all the levels [see Eq. (5)] and will be dominated by n_{11}. To explain fully we would have to consider also the variation of all the levels as well as the scattering rates $\omega_{i,f}$.

The gain G_m is given as[35]

$$G_m = \Gamma \frac{4\pi e^2 \langle z_{i,f} \rangle^2 (n_i - n_f)}{\epsilon_0 n \lambda L_p 2\gamma}, \tag{6}$$

where λ is the laser emission wavelength, 2γ is the experimental full width at half maximum (FWHM) of the electroluminescence spectrum below threshold, n is the mode refractive index, ε_0 is the permittivity of free space, L_p is the length of one period of the semiconductor structure (injector and active region), Γ is the overlap factor between the optical mode and the core active region, $\langle z_{i,f} \rangle$ is the radiative transition matrix element between the states i and f, and n_i and n_f are the populations of the subbands i and f, respectively. The variation of the gain for the transition $11 \rightarrow 9$ with applied electric field for the temperature $T_l = 300$ K is depicted in Fig. 4. The results for the lattice temperature $T_l = 77$ K are broadly of similar shape.

The sharp variation of the gain profile around an applied field of $F = 45.5$ kV/cm can be explained with reference to Eq. (6) and to Fig. 2, where we have previously noted the rapid change in n_{11} around this value of applied field. To account fully for the behavior of the gain profile with applied field, we would need to examine the variation of the radiative transition matrix element.

Also shown in the figure is the threshold gain g_{th} given in terms of the waveguide and mirror losses as
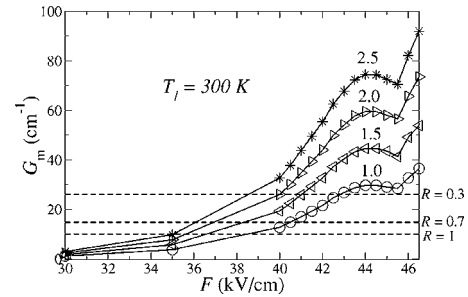

FIG. 4. The variation of the gain profile for the transition $11 \rightarrow 9$ with doping density. The doping densities are marked in the figure in units of 10^{17} cm^{-3}.

$$g_{th} = \alpha + \frac{1}{2L} \ln\left(\frac{1}{R_1 R_2} \right), \tag{7}$$

where α is the waveguide loss (measured by Beck *et al.*[9] as 10 cm^{-1}), L is the length of the cavity, and R_1 and R_2 are reflectivities of the mirrors taken equal to R, for values 1.0 (corresponding to perfect mirrors), 0.7 (the value quoted by Beck *et al.*), and 0.3 (arbitrarily chosen for comparison). We notice a significant variation with doping density.

Of particular interest is the injection efficiency η given as the ratio of the current to a particular active region level from the injector levels to the total current. This variation of η with applied field is shown in Fig. 5, where we show results for injection into the upper laser level, η_{11}, and also leakage from the lower laser level, η_9, for the lattice temperatures $T_l = 77$ and 300 K and for a doping density of $N_d = 2 \times 10^{17}$ cm^{-3}. It was noticed that the variation with doping density was marginal for a lattice temperature of 300 K and only slightly more significant for 77 K. We note that η_{11} is approximately 55% for the estimated working field of $F = 43$ kV/cm and decreases to approximately 45% for the field $F = 46$ kV/cm. The result for η_9 shows a gradual increase with field.

We discuss the injection efficiency for the upper laser level, η_{11}, in particular, noting the low value compared with the hoped-for value of unity. This can be explained by noting that injection into other levels is significant. In particular, we find that there is appreciable leakage directly to the active region levels $|4\rangle$, $|6\rangle$, $|8\rangle$, $|9\rangle$, and $|12\rangle$. For example, the injection directly to level $|12\rangle$ is appreciable at nearly 11%.
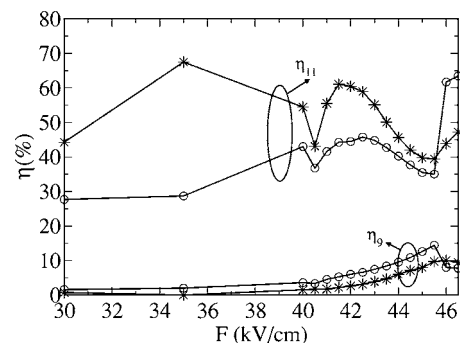

FIG. 5. Variation of the efficiency η for the upper and lower laser levels with applied electric field and with temperature ($\circ$ $T_l = 77$ K, $\star$ $T_l = 300$ K) for a doping density $N_d = 2 \times 10^{17}$ cm^{-3}.
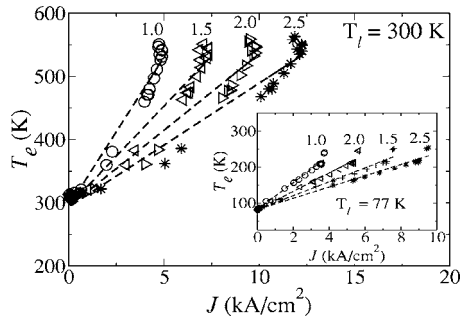
FIG. 6. The variation of the calculated electron temperature T_e with current density J and its dependence on doping density N_d and lattice temperature T_l. The dotted lines show the best fit approximation to the data and the doping densities are marked in the figure in units of 10^{17} cm^{-3}.

FIG. 7. The dependence of α_{e-l} with doping density.

Referring to Fig. 1, we can explain this by noting that the injector levels $|20\rangle$ and $|23\rangle$ have energies larger than the active region levels $|11\rangle$ and $|12\rangle$, so that we might expect that transitions to these action region levels will be appreciable, particularly at higher temperatures. This is in contrast to, for example, the active region level $|13\rangle$, for which only the injector level $|23\rangle$ has a larger energy, inhibiting the transition $|20\rangle \rightarrow |13\rangle$.

Of further interest is the behavior of the injection efficiency around $F = 45.5$ kV/cm, where we observe a rapid increase in η_{11}. This occurs around the region of NDR (see Fig. 3) and is presumably related to this (the efficiency involves the ratio of two currents and so is not so easy to describe). The behavior around $F = 40.5$ kV/cm is more difficult to explain since it would involve consideration of both the current into the upper laser level and the total current.

We now discuss our results for the electron temperature of the nonequilibrium electron distribution. Physically, it is argued that at large injected current densities, the power given to the excited electron system exceeds the rate at which the electrons relax and a nonequilibrium electron ensemble with an energy higher than the thermal reservoir is created. This continues until a steady-state is attained and the electron temperature reaches a steady value, see Ref. 33. Our results are presented in Fig. 6, where we follow Harrison et al.,[27] and consider the variation of the electron temperature T_e with the current density J, also considering its dependence with the doping density N_d and the lattice temperature T_l.

Figure 6 gives our results for the variation of electron temperature with current density for the four doping densities being considered for a lattice temperature of 300 K, while the inset shows the results for a lattice temperature of 77 K.

Following Ref. 27 we consider the possibility of a linear relationship between T_e and J and define the coupling constant α_{e-l} by the equation

$$T_e = T_l + \alpha_{e-l}J. \tag{8}$$

The results for α_{e-l}, defined by Eq. (8), and its dependence on the doping density and lattice temperature are shown in Fig. 7.

From this figure we note the decrease of α_{e-l} with doping density, implying that as we increase the doping density the
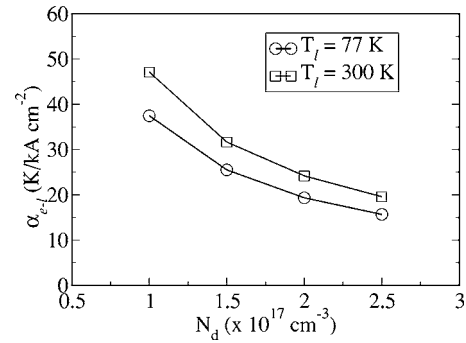
smaller we expect the electron temperature for a given current density. We also note that as the lattice temperature decreases then the smaller α_{e-l} becomes, and so the smaller the differences we expect between lattice and electron temperatures to be. This is in agreement with the experimental results of Troccoli et al.[32]

In these figures we also show the best fit lines to the data. We note that the linearity seems better for smaller lattice temperatures (agreeing with the comments of Ref. 27). Also we estimate $\alpha_{e-l} \approx 20$–50 K cm^2/kA for the range of doping densities considered, larger than the values quoted for the GaAs/AlGaAs devices discussed in Ref. 27 and comparable with those reported by Kohler et al.[12] This may be indicative of the important role of electron-electron scattering in this device or of the influence of the material system on T_e, in particular, the barrier material.

As can be determined from Fig. 7, the product $\alpha_{e-l}N_d$ is almost constant for both curves, suggesting an inverse relationship between α_{e-l} and N_d. We have

$$\alpha_{e-l}N_d \approx (38.5 \pm 0.7) \times 10^{17} \text{ K/kA cm} \quad (T_l = 77 \text{ K})$$

$$\approx (48.0 \pm 2) \times 10^{17} \text{ K/kA cm} \quad (T_l = 300 \text{ K}).$$

V. CONCLUSIONS

We have presented a detailed study of the impact of injector doping densities on the performance of InGaAs/InAlAs QCLs, our simulations including a self-consistent treatment of the subband population rate equations and accounting for all electron-longitudinal-optical phonon and electron-electron scattering rates. We found that the emission and absorption lifetimes deduced from our full self-consistent model differed from single particle estimates. The single particle estimates are often quoted, thus emphasizing the need for detailed modeling to extract the physics of these devices accurately.

We also included in our analysis the temperature of the nonequilibrium electron distribution and found that this differed significantly from the lattice temperature. We also noted that this temperature increased with the applied electric field and the current density, with coupling constants somewhat larger than in analogous GaAs based midinfrared QCLs.

The rather low injection efficiency to the upper lower laser level was noted and explained by noting the importance

of the coupling of the injector region levels to the other active region levels and the relative positions of the injector and active region energies.

Finally, our estimates for the coupling constant $\alpha_{e\text{-}l}$ relating the electron temperature T_e to the current density J gave values of approximately $20-50$ K cm^2/kA for the range of doping densities considered, somewhat larger than the values quoted for the GaAs/AlGaAs devices discussed in Ref. 27 and comparable with those reported by Kohler *et al.*[12] This may be indicative of the important role of electron-electron scattering in this device or of the influence of the material system on T_e, in particular, the barrier material.

[1]J. Faist, F. Capasso, D. L. Sivco, C. Sirtori, A. L. Hutchinson, and A. Y. Cho, Science **264**, 553 (1994).

[2]F. Capasso, C. Gmachl, D. L. Sivco, and A. Y. Cho, Phys. Today **55**(5) 34 (2002).

[3]C. Sirtori, Nature (London) **417**, 132 (2000).

[4]R. F. Kazarinov and R. A. Suris, Sov. Phys. Semicond. **5**, 707 (1971).

[5]R. F. Kazarinov and R. A. Suris, Sov. Phys. Semicond. **6**, 120 (1972).

[6]C. Gmachl, A. Trediccuci, D. L. Sivco, A. L. Hutchinson, F. Capasso, and A. Y. Cho, Science **286**, 749 (1999).

[7]C. Gmachl, D. L. Sivco, J. N. Baillargeon, A. L. Hutchinson, F. Capasso, and A. Y. Cho, Appl. Phys. Lett. **79**, 572 (2001).

[8]C. Gmachl, D. L. Sivco, R. Colombelli, F. Capasso, and A. Y. Cho, Nature (London) **415**, 883 (2002).

[9]M. Beck, D. Hofstetter, T. Aellen, J. Faist, U. Oesterle, M. Ilegems, E. Gini, and H. Melchior, Science **295**, 301 (2002).

[10]A. Evans, J. S. Yu, J. David, L. Doris, K. Mi, S. Slivken, and M. Razeghi, Appl. Phys. Lett. **84**, 314 (2004).

[11]A. Evans, J. S. Yu, S. Slivken, and M. Razeghi, Appl. Phys. Lett. **85**, 2166 (2004).

[12]R. Kohler *et al.*, Nature (London) **417**, 156 (2002).

[13]J.-Y. Bengloan, A. De Rossi, V. Ortiz, X. Marcadet, M. Calligaro, I. Maurin, and C. Sirtori, Appl. Phys. Lett. **84**, 2019 (2004).

[14]C. Gmachl, A. Belyanin, D. L. Sivco, M. L. Peabody, N. Owschimikow, A. M. Sergent, F. Capasso, and A. Y. Cho, IEEE J. Quantum Electron. **39**, 1345 (2003).

[15]T. S. Mosely, A. Belyanin, C. Gmachl, D. L. Sivco, M. L. Peabody, and A. Y. Cho, Opt. Express **12**, 2972 (2004).

[16]M. Troccoli, A. Belyanin, F. Capasso, E. Cubukcu, D. L. Sivco, and A. Y. Cho, Nature (London) **433**, 845 (2005).

[17]M. Giehler, R. Hey, H. Kostial, S. Cronenberg, T. Ohtsuka, L. Schrottke, and H. T. Grahn, Appl. Phys. Lett. **82**, 671 (2003).

[18]S.-C. Lee, M. Giehler, R. Hey, T. Ohtsuka, A. Wacker, and H. T. Grahn, Semicond. Sci. Technol. **19**, S45 (2004).

[19]M. Giehler, H. Kostial, R. Hey, and H. T. Grahn, J. Appl. Phys. **96**, 4755 (2004).

[20]Y. Hirayama, J. H. Smet, L. H. Peng, C. G. Fonstad, and E. P. Ippen, Jpn. J. Appl. Phys., Part 1 **33**, 89 (1994).

[21]*Semiconductors: Basic Data*, 2nd ed., edited by O. Madelung (Springer, Berlin, 1996).

[22]J. M. Cole, L. G. Earwaker, A. G. Cullis, N. G. Chew, and S. J. Bass, J. Appl. Phys. **60**, 2639 (1986).

[23]D. Indjin, P. Harrison, R. W. Kelsall, and Z. Ikonić, J. Appl. Phys. **91**, 9019 (2002).

[24]G. A. Bastard, *Wave Mechanics Applied to Semiconductor Heterostructures* (Les Editions de Physique, Paris, 1988).

[25]J. H. Smet, C. G. Fonstad, and Q. Hu, J. Appl. Phys. **79**, 9305 (1996).

[26]K. Donovan, P. Harrison, R. W. Kelsall, and P. Kinsler, *Proceedings of Sixth IEEE International Conference on Terahertz Electronics, Leeds, UK, 3–4 September 1998*, (IEEE, New York, 1998), pp. 223–226.

[27]P. Harrison, D. Indjin, and R. W. Kelsall, J. Appl. Phys. **92**, 6921 (2002).

[28]Z. Ikonić, R. W. Kelsall, and P. Harrison, Phys. Rev. B **69**, 235308 (2004).

[29]Z. Ikonić, R. W. Kelsall, and P. Harrison, J. Appl. Phys. **96**, 6803 (2004).

[30]G. Scamarcio, F. Capasso, C. Sirtori, J. Faist, A. L. Hutchinson, D. L. Sivco, and A. Y. Cho, Science **276**, 773 (1997).

[31]R. Bates *et al.*, Appl. Phys. Lett. **83**, 4092 (2003).

[32]M. Troccoli, G. Scamarcio, V. Spagnolo, A. Trediccuci, C. Gmachl, F. Capasso, D. L. Sivco, and M. Striccoli, Appl. Phys. Lett. **77**, 1088 (2000).

[33]P. Harrison *et al.*, Phys. Status Solidi A **202**, 980 (2005).

[34]M. Giovannini, T. Aellen, T. Gresch, R. Maulini, J.-M. Bulliard, L. Sirigu, N. Hoyler, and J. Faist, 13th International Conference on Molecular Beam Epitaxy (MBE 2004), Edinburgh, Scotland, UK, 22–24 August 2004 (unpublished).

[35]C. Sirtori, J. Faist, F. Capasso, D. L. Sivco, A. L. Hutchinson, S. N. G. Chu, and A. Y. Cho, Appl. Phys. Lett. **68**, 1745 (1996).